PNAS RESEARCH ARTICLE | BIOPHYSICS AND COMPUTATIONAL BIOLOGY OPEN ACCESS

# Direct observation of stepping rotation of V-ATPase reveals rigid component in coupling between $V_o$ and $V_1$ motors

Akihiro Otomo[a,b], Tatsuya Iida[a,b], Yasuko Okuni[a], Hiroshi Ueno[c], Takeshi Murata[d], and Ryota Iino[a,b,1]

Edited by Stephan Wilkens, State University of New York Upstate Medical University, Syracuse, NY; received June 22, 2022; accepted September 13, 2022 by Editorial Board Member Yale E. Goldman

**V-ATPases are rotary motor proteins that convert the chemical energy of ATP into the electrochemical potential of ions across cell membranes. V-ATPases consist of two rotary motors, $V_o$ and $V_1$, and *Enterococcus hirae* V-ATPase ($EhV_oV_1$) actively transports $Na^+$ in $V_o$ ($EhV_o$) by using torque generated by ATP hydrolysis in $V_1$ ($EhV_1$). Here, we observed ATP-driven stepping rotation of detergent-solubilized $EhV_oV_1$ wild-type, aE634A, and BR350K mutants under various $Na^+$ and ATP concentrations ($[Na^+]$ and [ATP], respectively) by using a 40-nm gold nanoparticle as a low-load probe. When $[Na^+]$ was low and [ATP] was high, under the condition that only $Na^+$ binding to $EhV_o$ is rate limiting, wild-type and aE634A exhibited 10 pausing positions reflecting 10-fold symmetry of the $EhV_o$ rotor and almost no backward steps. Duration time before the forward steps was inversely proportional to $[Na^+]$, confirming that $Na^+$ binding triggers the steps. When both [ATP] and $[Na^+]$ were low, under the condition that both $Na^+$ and ATP bindings are rate limiting, aE634A exhibited 13 pausing positions reflecting 10- and 3-fold symmetries of $EhV_o$ and $EhV_1$, respectively. The distribution of duration time before the forward step was fitted well by the sum of two exponential decay functions with distinct time constants. Furthermore, occasional backward steps smaller than 36° were observed. Small backward steps were also observed during three long ATP cleavage pauses of BR350K. These results indicate that $EhV_o$ and $EhV_1$ do not share pausing positions, $Na^+$ and ATP bindings occur at different angles, and the coupling between $EhV_o$ and $EhV_1$ has a rigid component.**

V-ATPase | single-molecule analysis | molecular motors

## Significance

V-ATPases are ion pumps consisting of two rotary motor proteins, $V_o$ and $V_1$, that actively transport ions across the cell membrane using the chemical energy of ATP. To understand how V-ATPases transduce the energy in the presence of a structural symmetry mismatch between $V_o$ and $V_1$, we simultaneously visualized the rotational pauses and forward and backward steps of $V_o$ and $V_1$ coupled with ion transport and ATP hydrolysis reactions, respectively. Our results suggest that V-ATPases with multiple peripheral stalks are more rigidly coupled than F-ATPases that have only one peripheral stalk and work as ATP synthases. Our high-speed/high-precision single-molecule imaging of rotary ATPases in action will pave the way for a comprehensive understanding of their energy transduction mechanisms.

Rotary ATPases are ubiquitously expressed in living organisms and play important roles in biological energy conversions (1–6). These rotary ATPases are classified into F-, V-, and A-ATPases based on their amino acid sequences and physiological functions (6). Eukaryotic and bacterial F-ATPases ($F_oF_1$) and archaeal A-ATPases ($A_oA_1$) mainly function as ATP synthases driven by the electrochemical potential of ions across the cell membrane, although they can also act as active ion pumps driven by ATP hydrolysis depending on the cellular environment. In contrast, V-ATPases ($V_oV_1$) in eukaryotes primarily function as active ion pumps. V-ATPases are also found in bacteria, and some of them are termed V/A-ATPases based on their origin and physiological function in ATP synthesis (6–8).

To date, numerous studies have been conducted to understand how the two motor proteins (i.e., $F_1/A_1/V_1$ and $F_o/A_o/V_o$) of the rotary ATPases couple their rotational motions and functions. Single-molecule studies using fluorescent probes (9–12), gold nanoparticle (AuNP) or nanorod probes (13–21), and Förster resonance energy transfer (16, 22, 23) have revealed the rotational dynamics of rotary ATPases for both ATP hydrolysis/synthesis directions. Furthermore, recent cryo–electron microscopic (cryo-EM) single-particle analyses have revealed entire architectures of the rotary ATPases with different structural states at atomic resolutions (24–35). In particular, several studies have demonstrated elastic coupling of $F_oF_1$ due to large deformations of the peripheral stalk connecting $F_o$ and $F_1$ (25, 29, 35). However, few studies on other types of rotary ATPases with different functions and subunit compositions have been performed, and a comprehensive understanding of the energy transduction mechanism remains elusive.

*Enterococcus hirae* V-ATPase ($EhV_oV_1$) works as an ATP-driven sodium ion ($Na^+$) pump to maintain $Na^+$ concentrations ($[Na^+]$) inside the cell (Fig. 1*A*) (37–41). Note that we use the term V-ATPase or $V_oV_1$ because its physiological function is not ATP synthesis but active ion transport. $EhV_oV_1$ is a multisubunit complex composed of nine different subunits, namely, $ac_{10}dE_2G_2$ and $A_3B_3DF$ complexes in $EhV_o$ and $EhV_1$, respectively. In the $EhV_1$ $A_3B_3DF$ complex, three pairs of the A and B subunits form a heterohexameric $A_3B_3$ stator ring, and the central rotor DF subcomplex is inserted into the $A_3B_3$ ring (Fig. 1*B*, *Bottom*) (42, 43). The $EhV_o$ $ac_{10}dE_2G_2$ complex

Author contributions: A.O., H.U., T.M., and R.I. designed research; A.O., T.I., and Y.O. performed research; T.I., Y.O., H.U., and T.M. prepared samples; A.O. analyzed data; and A.O. and R.I. wrote the paper.

The authors declare no competing interest.

This article is a PNAS Direct Submission. S.W. is a guest editor invited by the Editorial Board.



[1]To whom correspondence may be addressed. Email: iino@ims.ac.jp.

This article contains supporting information online at http://www.pnas.org/lookup/suppl/doi:10.1073/pnas.2210204119/-/DCSupplemental.

Published October 10, 2022.

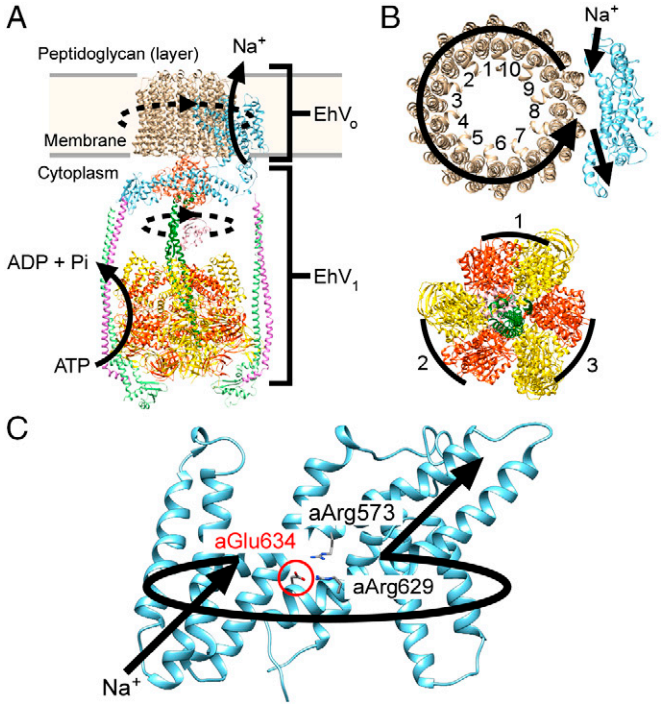


**Fig. 1.** (*A*) Overall architecture of $EhV_oV_1$. The dotted circular arcs represent the rotation direction driven by ATP hydrolysis. (*B*) (*Top*) Top view of the a subunit (cyan) and $c_{10}$ ring (brown) of $EhV_o$ and (*Bottom*) A (yellow), B (orange), D (green), and F subunits (pink) of $EhV_1$. The black arrow in *Top* indicates the path of $Na^+$ movement during ATP-driven rotation. The arcs in *Bottom* represent the catalytic AB pairs. (*C*) Side view of the a subunit viewed from the c subunit. This structure was constructed by the SWISS-MODEL server (36) using a structure of the a subunit of V-ATPase from *T. thermophilus*. The black arrows represent the path of $Na^+$ movement during ATP-driven rotation. The mutated residue, aGlu634, is located on the surface of the entry half-channel of the a subunit as highlighted in red letters and a circle.

transports $Na^+$ across the cell membrane. The membrane-embedded rotor ring is formed by a decamer of the tetrahelical transmembrane c subunit ($c_{10}$ ring; Fig. 1*B*, *Top*) connected with the central DF stalk via the d subunit (26, 44). The stator a subunit works as an ion channel, and two EG peripheral stalks interact with the a subunit and $A_3B_3$ ring to assure rotary coupling between $EhV_o$ and $EhV_1$.

In $EhV_1$, the ATP hydrolysis reaction is catalyzed at the interfaces of three A and B subunits. It drives a counterclockwise rotation of the DF rotor subunits as viewed from the $EhV_o$ side (Fig. 1*B*, *Bottom*). Like other $F_1/A_1/V_1$ (11, 45), $EhV_1$ is a stepping motor that rotates 120° per one ATP hydrolysis (46). We previously revealed that the 120° step of isolated $EhV_1$ is further divided into 40 and 80° substeps by using high-speed and high-precision single-molecule imaging analysis with AuNP as a low-load probe (47). A main pause before the 40° substep involves ATP cleavage, phosphate release, and ATP binding events. The ATP binding triggers the 40° substep because the duration time is inversely proportional to [ATP]. The 80° substep is triggered by ADP release after a subpause with [ATP]-independent duration time. While the chemomechanical coupling scheme in $EhV_1$ has been revealed, because our previous single-molecule observation of $EhV_oV_1$ did not clearly resolve the pauses and steps (17), the elementary steps in the rotation of $EhV_oV_1$ have not been revealed.

Although the mechanism of ion transport in $F_o/A_o/V_o$ is not fully understood, the so-called "two-channel" model has been widely accepted (48–54). In this model, the a-subunit has two half-channels for ion entry/exit into/from the ion-binding sites of the rotor c ring. In the case of $EhV_o$, $Na^+$ enters the half-channel from the cytoplasmic side and binds to the negatively charged $Na^+$-binding sites of the c subunit (44, 55). Then, the charge-neutralized c subunit can move into the hydrophobic lipid membrane (53, 56). The rotational torque generated by ATP hydrolysis in $EhV_1$ is transmitted to $EhV_o$ via the rotor d subunit, allowing the $c_{10}$ ring to rotate unidirectionally in the lipid membrane. $Na^+$ translocated by a nearly single turn of the $c_{10}$ ring reaches another half-channel of the a subunit, which connects the $Na^+$-binding site of the c subunit to the extracellular side. Then, $Na^+$ is pumped out of the cell by a hydrated microenvironment (57) and/or electrostatic repulsion with the positively charged residues in the a subunit, aArg573 and aArg629, located at the interface between the two half-channels (Fig. 1*C* and *SI Appendix*, Fig. S1) (26). Because $EhV_oV_1$ has the $c_{10}$ ring, 10 $Na^+$ are transported per single turn. Therefore, the step size of $EhV_o$ is expected to be 36° (360°/10), similar to *Escherichia coli* and yeast $F_oF_1$, which also have $c_{10}$ rings (13, 14, 22, 35).

The ion-to-ATP ratio is a central issue in the coupling mechanism of rotary ATPases. All known $F_1/A_1/V_1$ have three catalytic sites and threefold structural symmetry and hydrolyze or synthesize three ATP molecules per single turn. In contrast, the number of protomers forming the rotor c ring of $F_o/A_o/V_o$ varies from 8 to 17 depending on the species, suggesting wide variations in the ion-to-ATP ratio of rotary ATPases (58, 59). In $EhV_oV_1$, because the rotor c ring of $EhV_o$ has a 10-fold structural symmetry (Fig. 1*B*, *Top*), this enzyme has a structural symmetry mismatch and a noninteger ratio between transported $Na^+$ and hydrolyzed ATP (10/3 = 3.3). If the rotational coupling between $EhV_o$ and $EhV_1$ is elastic, as reported for *E. coli* and yeast $F_oF_1$, the symmetry mismatch is relieved by large deformations of the peripheral stalk and/or the central rotor (25, 29, 35, 60). On the other hand, if the coupling is rather rigid due to the multiple peripheral stalks of $EhV_oV_1$, the pausing positions of both $EhV_o$ and $EhV_1$ would be observed independently in a single-molecule observation. To address this issue, it is required to directly visualize the rotational pauses and steps of $EhV_oV_1$ under conditions where the elementary steps of the rotation such as the bindings of $Na^+$ and ATP to $EhV_o$ and $EhV_1$, respectively, are both rate-limiting.

Here we carried out high-speed and high-precision single-molecule imaging of the rotation of detergent-solubilized $EhV_oV_1$ by using 40-nm AuNP as a low-load probe. To resolve the rotational pauses and steps of $EhV_o$, a glutamate residue in the stator a subunit (aGlu634) was replaced with alanine. Since the mutated aGlu634 is located on the surface of the $Na^+$ entry half-channel (Fig. 1*C* and *SI Appendix*, Fig. S2), $Na^+$ binding to the c subunit in the $EhV_oV_1$(aE634A) mutant (hereinafter referred to as aE634A) is expected to become slower than in the wild type. The rotation rate of aE634A decreased about 10 times compared with that of the wild type, allowing us to clearly resolve the rotational pauses and steps in $EhV_o$. Under the condition that only $Na^+$ binding is rate-limiting, aE634A showed 10 pausing positions per single turn and a step size of about 36°, consistent with 10 protomers in the $c_{10}$ ring of $EhV_o$. The duration time before the forward step was inversely proportional to [$Na^+$], indicating that the dwell corresponds to the waiting time for $Na^+$ binding. On the other hand, under the condition that both $Na^+$ and ATP bindings are rate-limiting, 13 pausing positions per single turn were observed. Furthermore, backward steps smaller than 36° were occasionally observed only when ATP binding is also rate-limiting,

indicating that $EhV_oV_1$ undergoes Brownian motion between adjacent pausing positions of $EhV_o$ and $EhV_1$ when no torque is applied from $EhV_1$. Backward steps of 36° or larger than 36° were rarely observed, suggesting the suppression of reverse $Na^+$ transport. Small backward steps were also frequently observed during three long ATP cleavage pauses of another mutant, $EhV_oV_1$(BR350K), in which ATP hydrolysis is rate-limiting for the rotation (47). From these results, we conclude that $EhV_o$ and $EhV_1$ do not share their pausing positions, $Na^+$ and ATP bindings occur at different angles, and their coupling has a rigid component.

## Results

**[ATP] and [$Na^+$] Dependence of Rotation Rate of Wild Type and aE634A.** To clearly visualize the ATP-driven rotation rate-limited by $Na^+$ transport, site-directed mutagenesis was conducted on the a subunit of $EhV_o$ (aE634A). The purified aE634A solubilized with *n*-dodecyl-β-D-maltoside (DDM) exhibited subunit stoichiometry similar to the wild type in SDS-PAGE (*SI Appendix*, Fig. S3), indicating intactness of the complex.

Fig. 2*A* draws a schematic illustration of single-molecule observation. In this system, the ATP-driven rotation of $V_oV_1$, immobilized on a glass surface, was probed by AuNPs attached to the A subunit via biotin–streptavidin conjugation (*SI Appendix*). The localization precision in this system was 0.6 nm at 3,000 frames per second (fps) (0.33 ms temporal resolution) as determined by centroid analysis of the scattering images of single AuNPs non-specifically attached to the glass surface (*SI Appendix*, Fig. S4).

The rotation rates of the wild type and aE634A at various substrate concentrations were examined from the slope of the time course of rotation (Fig. 2 *B* and *C* and *SI Appendix*, Fig. S5). [ATP] dependences of the rotation rate for the wild type and aE634A in the presence of 300 mM $Na^+$ are shown in Fig. 2*B*. Under this high-[$Na^+$] condition, $Na^+$ binding is fast and not rate-limiting, and consequently, [ATP] dependence obeyed Michaelis–Menten kinetics. Obtained kinetic parameters, the Michaelis constant ($K_m^{ATP}$) and the maximum velocity ($V_{max}^{ATP}$), are summarized in Table 1. The value of $K_m^{ATP}$ for the wild type was 60.4 ± 2.1 μM (fitted value ± SE of the fit). This value was comparable to that for the isolated $EhV_1$ (43 ± 6 μM), indicating that the apparent affinity of ATP was not significantly affected by $EhV_o$. On the other hand, the value of $V_{max}^{ATP}$ (40.0 ± 0.3 rps, fitted value ± SE of the fit) was significantly smaller than that of the isolated $EhV_1$ (117 ± 3 rps) (47). As a result, the binding rate constant of ATP ($k_{on}^{ATP}$) as estimated by $3 \times V_{max}^{ATP}/K_m^{ATP}$ was smaller than that of the isolated $EhV_1$ (Table 1). We attributed this difference to the intact interaction between the rotor $c_{10}$ ring and stator a subunit of $EhV_o$ and concluded that $Na^+$ transport in $EhV_o$ limits the $V_{max}^{ATP}$ of $EhV_oV_1$, as discussed in our previous single-molecule study (17). In aE634A, the values of $K_m^{ATP}$ and $V_{max}^{ATP}$ were 6.6 ± 0.3 μM and 4.58 ± 0.04 rps, respectively, and both were approximately one-tenth of those of the wild type (Table 1). Thus, the $k_{on}^{ATP}$ for aE634A ($2.1 \times 10^6$ $M^{-1}$ $s^{-1}$) was in close agreement with that for the wild type ($2.0 \times 10^6$ $M^{-1}$ $s^{-1}$) (Table 1). These results indicate that the mutation in aGlu634 affects only $Na^+$ transport and not ATP binding in the $EhV_oV_1$ complex.

Fig. 2*C* shows [$Na^+$] dependence of the rotation rate at saturated [ATP] (5 mM). Here contaminating $Na^+$ in the observation buffers was estimated by an inductivity coupled plasma optical emission spectrometer (ICP-OES) (*SI Appendix*, Fig. S6), and total [$Na^+$] including contamination was used for the plot. Under this condition, [ATP] is sufficiently high, ATP binding is not rate-limiting (Fig. 2*B* and Table 1), and the effect of [$Na^+$] on the rotation rate becomes obvious. As a result, both the wild type and aE634A showed biphasic responses to [$Na^+$]. As reported in our previous studies, data were fitted by a summation of two independent Michaelis–Menten equations assuming two $Na^+$ binding sites (17, 61). The obtained kinetic parameters are shown in Table 2. Both values of $V_{max1}^{Na}$ and $V_{max2}^{Na}$ for aE634A (1.1 ± 0.3 and 4.4 ± 0.5 rps, fitted value ± SE of the fit) were about 10 times smaller than those for the wild type (15.7 ± 1.6 and 35.0 ± 7.1 rps) (Table 2). On the other hand, considering the large fitting error, especially in the wild type, the values of $K_{m1}^{Na}$ and $K_{m2}^{Na}$ do not seem to be significantly different between aE634A (0.32 ± 0.28 and 58.3 ± 26.5 mM,

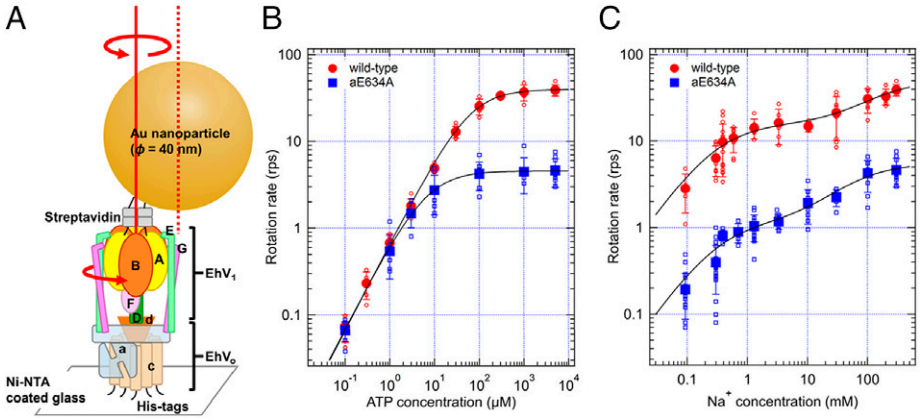


**Fig. 2.** (*A*) Schematic model of the single-molecule rotation assay of $EhV_oV_1$ probed with AuNP. Each letter represents the name of the subunits. $EhV_oV_1$ was fixed on $Ni^{2+}$-NTA–coated cover glass via $His_3$ tags added to the C terminus of the c subunit. A streptavidin-coated gold nanoparticle (40 nm in diameter) was attached to the N terminus of the A subunit, which was biotinylated by adding an Avi-tag. Solid and dotted red lines indicate the center axis of $EhV_oV_1$ and the centroid of the attached AuNP, respectively. Because the rotor $c_{10}$ ring was fixed on a glass surface, the stator subunits rotate counterclockwise against the rotor subunits as shown by red arrows. (*B*) [ATP] dependence of the rotation rate of wild type and aE634A at 300 mM NaCl. Red open circles and blue open squares indicate the data from individual molecules of wild type and aE634A, respectively. The closed symbols are averages, and error bars represent SDs. Data were fitted with the Michaelis–Menten equation: $V = V_{max}^{ATP} \cdot [ATP]/(K_m^{ATP} + [ATP])$. The obtained kinetic parameters are summarized in Table 1. (*C*) [$Na^+$] dependence of rotation rate of wild type and aE634A at 5 mM ATP. The correspondence of colored symbols is the same as in *B*. The black lines show the fit with the sum of two independent Michaelis–Menten equations: $V = V_{max1}^{Na} \cdot [Na^+]/(K_{m1}^{Na} + [Na^+]) + V_{max2}^{Na} \cdot [Na^+]/(K_{m2}^{Na} + [Na^+])$. The obtained kinetic parameters are summarized in Table 2. The contaminating $Na^+$ in the observation buffers was taken into account as shown in *SI Appendix*, Fig. S6. Namely, 50 mM Bis-Tris (pH 6.5) was used for 0.09 mM $Na^+$, and 20 mM potassium phosphate (pH 6.5) was used for the other [$Na^+$] values as buffers.

**Table 1. Kinetic parameters for [ATP] dependence of rotation rate of $EhV_oV_1$ and $EhV_1$**

| Protein | NaCl (mM) | $K_m^{ATP}$ (μM) | $V_{max}^{ATP}$ (rps) | $k_{on}^{ATP}$* ($M^{-1}$ $s^{-1}$) | Reference |
|---|---|---|---|---|---|
| $EhV_oV_1$ wild type | 300 | 60.4 ± 2.1 | 40.0 ± 0.3 | $2.0 \times 10^6$ | This study (single molecule) |
| $EhV_oV_1$ aE634A | 300 | 6.6 ± 0.3 | 4.58 ± 0.04 | $2.1 \times 10^6$ | This study (single molecule) |
| $EhV_oV_1$ wild type | 300 | 134 ± 12 | 59 ± 1 | $1.3 \times 10^6$ | Ref. 17 (biochemical) |
| $EhV_1$ wild type | 0 (50 mM KCl) | 43 ± 6 | 117 ± 3 | $8.2 \times 10^6$ | Ref. 47 (single molecule) |

*The binding rate constant of ATP estimated by $k_{on}^{ATP} = 3 \times V_{max}^{ATP}/K_m^{ATP}$.

fitted value ± SE of the fit) and the wild type (0.29 ± 0.09 and 160.2 ± 88.8 mM). Then, the binding rate constant of $Na^+$ ($k_{on}^{Na}$) as estimated by $10 \times V_{max}^{Na}/K_m^{Na}$ largely decreased in aE634A, notably more than 10 times for the high-affinity site ($k_{on1}^{Na}$; Table 2). The significant decrease in the $V_{max2}^{Na}$ for aE634A compared with that of the wild type also suggests that the rate of elementary reaction steps other than $Na^+$ binding also decreased in $EhV_o$. Because $Na^+$ binding to $EhV_o$ is certainly rate-limiting at low [$Na^+$] for both the wild type and aE634A, we then conducted a detailed analysis of the rotational pauses and steps at low [$Na^+$].

**Pauses and Steps of $EhV_o$ and $EhV_1$ in ATP-Driven Rotation of Wild Type and aE634A.** Fig. 3*A* and *SI Appendix*, Fig. S7 show typical time courses of the rotational trajectory (pink line) of the wild type observed at 0.3 mM $Na^+$ and 5 mM ATP with 3,000 fps (0.33 ms temporal resolution). An enlarged trajectory for a single revolution and corresponding *x*–*y* trajectory (Fig. 3*A*, *Inset*, pink line) are also shown. Under this condition, not ATP binding but $Na^+$ binding is rate-limiting of ATP-driven rotation (Fig. 2 *B* and *C* and Table 2). The rotational trajectory showed transient pauses and steps in a forward, counterclockwise direction. Then, the pauses and steps were objectively detected with a step-finding algorithm (62) (black line on the trajectory) applied to median-filtered traces (current ± 4 frames, red line), as in our previous studies on other motor proteins (63, 64). As indicated by the numbers in the trajectories, 10 pauses were mainly detected in a single turn (Fig. 4*A*), reflecting the number of protomers in the rotor $c_{10}$ ring (Fig. 1*B*, *Top*). In addition, numbers of pauses smaller or larger than 10 per single turn were also detected (Fig. 4*A*). A number of pauses smaller than 10 can be attributed to undetectable short pauses due to the limited time resolution because the stepping behavior is a stochastic process. A number of pauses larger than 10 is presumably due to occasional detection of the subpauses of $EhV_1$ for ADP release, which has a time constant of 2.5 ms and is independent of [ATP] (47). Furthermore, a small fraction of underfitting or overfitting of the step-finding algorithm would also be included (64). The distribution of the step size revealed that backward steps were rarely observed (0.8%; Fig. 3*B*), the average value of the forward step was 36.6°, and a Gaussian function fitted the distribution well with a peak at 33.8 ± 14.2° (peak ± SD). These values show excellent agreement with the step size expected from the structural symmetry of the $c_{10}$ ring (360°/10 = 36°). The distribution of duration time before the forward step was fitted well by a single exponential decay function with a time constant of 13.5 ± 0.3 ms (fitted value ± SE of the fit), indicating a single rate-limiting step of the rotation (Fig. 3*C*).

Rotational trajectories of aE634A observed at 0.3 mM $Na^+$ and 5 mM ATP with 1,000 fps are shown in Fig. 5*A* and *SI Appendix*, Fig. S8. In aE634A, the median filtering of current ± 7 frames was applied for the step-finding algorithm (62). As in the wild type, the number of pauses per single turn was mainly 10 (Fig. 4*B*), and the step size was 37.1° (average) or 34.9 ± 12.8° (peak ± SD) (Fig. 5*B*), consistent with the structural symmetry of the $c_{10}$ ring, and the ratio of backward steps was minor (1.2%). The distribution of duration time before the forward steps for aE634A was fitted well by a single exponential decay function with a time constant of 137 ± 6 ms (Fig. 5*C*), which is 10 times larger than that of the wild type, consistent with the analysis of the rotation rate (Fig. 2*C* and Table 2). For aE634A, we also examined [$Na^+$] dependence, and *SI Appendix*, Fig. S9 shows rotational trajectories at 0.09 or 1.3 mM $Na^+$ and 5 mM ATP. Distributions of the step size and the duration before the forward step at 0.09 and 1.3 mM $Na^+$ are shown in Fig. 6 *A*–*D*, respectively. As with 0.3 mM $Na^+$, step sizes of about 36° were obtained, indicating that the 36° step is independent of [$Na^+$]. In contrast, although distributions of duration time before the forward step were also fitted well by a single exponential decay function as with 0.3 mM $Na^+$, the time constants changed greatly. Fig. 6*E* shows [$Na^+$] dependence of the time constant. The slope was −1.1 when the data point at 1.3 mM $Na^+$ was excluded because it is the first saturating concentration observed in the rotation rate analysis (Fig. 2*C* and Table 2). If this data point was included, the slope was −1.0. Therefore, the time constant is almost inversely proportional to [$Na^+$], indicating that $Na^+$ binding is rate-limiting for the rotation. Furthermore, this result indicates that ATP hydrolysis in $EhV_1$ is tightly coupled with $Na^+$ transport in $EhV_o$ in the $EhV_oV_1$ complex solubilized with DDM.

Next, we observed the rotation of aE634A at 0.3 mM $Na^+$ and 1 μM ATP at 1,000 fps (Fig. 7*A* and *SI Appendix*, Fig. S10). Under this condition, both $Na^+$ and ATP bindings were rate-limiting for rotation (Fig. 2 *B* and *C*). The step-finding algorithm was applied to the median-filtered trace (current ± 7 frames, red line). As a result, the number of detected pauses in a single turn was mainly 13, reflecting 10 pausing positions of $EhV_o$ and 3 pausing positions of $EhV_1$ (Fig. 4*C*). This result indicates that the pausing positions waiting for $Na^+$ and ATP bindings are different in the $EhV_oV_1$ complex. The distribution

**Table 2. Kinetic parameters for [$Na^+$] dependence of rotation rate of wild type and aE634A**

| Protein | $K_{m1}^{Na}$ (mM) | $V_{max1}^{Na}$ (rps) | $k_{on1}^{Na}$* ($M^{-1}$ $s^{-1}$) | $K_{m2}^{Na}$ (mM) | $V_{max2}^{Na}$ (rps) | $k_{on2}^{Na}$* ($M^{-1}$ $s^{-1}$) |
|---|---|---|---|---|---|---|
| $EhV_oV_1$ wild type | 0.29 ± 0.09 | 15.7 ± 1.6 | $5.4 \times 10^5$ | 160.2 ± 88.8 | 35.0 ± 7.1 | $2.2 \times 10^3$ |
| $EhV_oV_1$ aE634A | 0.32 ± 0.28 | 1.1 ± 0.3 | $3.4 \times 10^4$ | 58.3 ± 26.5 | 4.4 ± 0.5 | $7.5 \times 10^2$ |

[ATP] was 5 mM.
*The binding rate constant of $Na^+$ estimated by $k_{on1(2)}^{Na} = 10 \times V_{max1(2)}^{Na}/K_{m1(2)}^{Na}$.

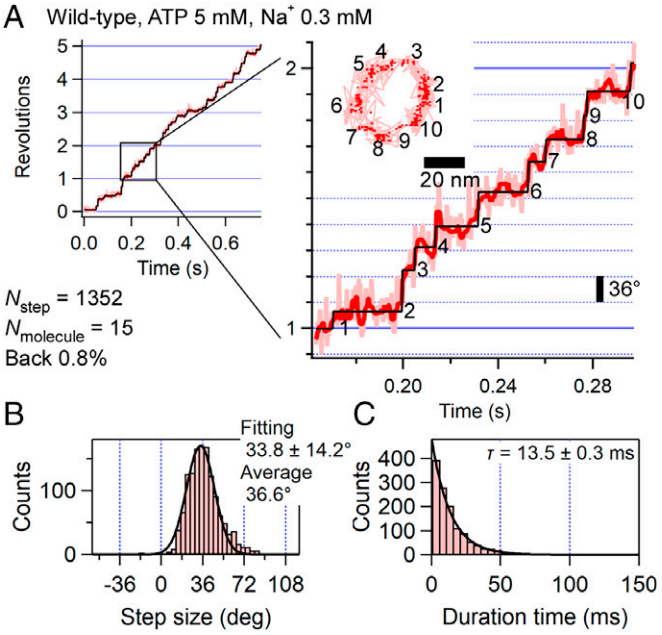


**Fig. 3.** (*A*) Typical trajectory of ATP-driven rotation of wild-type $EhV_oV_1$ at 5 mM ATP and 0.3 mM $Na^+$ recorded at 3,000 fps (0.33 ms time resolution). (*Right*) Enlarged view of one revolution (360°). Pink, red, and black traces represent raw, median-filtered (current ± 4 frames), and fitted trajectories, respectively. (*Inset*) The corresponding *x*-*y* trajectory. Pink lines and red dots represent the raw and median-filtered (current ± 4 frames) coordinates, respectively. We collected 1,352 steps from 15 molecules. Other examples of trajectories are shown in *SI Appendix*, Fig. S7. (*B*) Distribution of the step size fitted with a single Gaussian assuming a single peak. The values at the top right are the fitted parameter (peak ± SD) and average. The ratio of backward steps was 0.8%. (*C*) Distribution of the duration time before the forward step fitted with a single exponential decay function. The value at the top right is the obtained time constant (fitted value ± SE of the fit).

of the step size is shown in Fig. 7*B*. The average value for the forward step was 29.9°, which is distinctly smaller than 36°. When we superimposed the two histograms in Fig. 5*B* (0.3 mM $Na^+$ and 5 mM ATP) and Fig. 7*B* (0.3 mM $Na^+$ and 1 μM ATP) after normalizing the maximum values, the difference was obvious (*SI Appendix*, Fig. S11). Furthermore, interestingly, in contrast to the condition in which $Na^+$ binding was the sole rate-limiting factor, the ratio of the backward step increased to 6.1%. Therefore, we fitted the distribution with the sum of three Gaussians: one peak in the backward (minus) direction and two peaks in the forward (plus) direction. Note that one of the forward peaks was fixed at 36°, which is assumed as the step of $EhV_o$. Then, we obtained three peaks at −14.2 ± 6.8, 23.1 ± 10.4, and 36.0 ± 12.8° (peak ± SD; Fig. 7*B*). For comparison, the fitting with two Gaussians with peaks in minus and plus directions is shown in *SI Appendix*, Fig. S12*A*. The distribution of duration time before the forward step fitted better with the sum of two exponential decay functions (coefficient of determination $R^2 = 0.98$; Fig. 7*C*) than with a single exponential decay function ($R^2 = 0.94$; *SI Appendix*, Fig. S12*B*), and time constants of 135 ± 24 and 642 ± 322 ms (fitted value ± SE of the fit) were obtained. These values presumably correspond to the time constants for $Na^+$ and ATP bindings, respectively, because the time constant for $Na^+$ binding was 137 ms at 0.3 mM $Na^+$ and 5 mM ATP (Fig. 5*C*), and that for ATP binding was 476 ms at 1 μM ATP as estimated from $k_{on}^{ATP}$ ($2.1 \times 10^6$ $M^{-1}$ $s^{-1}$; Table 1). These results are consistent with the notion that both $Na^+$ and ATP bindings are rate-limiting for rotation.

**Backward and Recovery Steps between Adjacent Pauses of $EhV_o$ and $EhV_1$.** As described above, occasional backward steps (6.1% of total steps) were observed under conditions where both $Na^+$ and ATP bindings were rate-limiting for rotation (Fig. 7*B*). Typical examples of backward steps are shown in Fig. 8*A*. Green, cyan, and purple lines indicate the forward step just before the backward step, the backward step, and the forward step after the backward step (recovery step), respectively. Fig. 8 *B*–*D* shows the step size distributions for these events. The average value of a backward step size was −18.8° (Fig. 8*C*), which is smaller than the expected step size (36°) of $EhV_o$. Because backward steps were observed when not only $Na^+$ binding but also ATP binding was rate-limiting for rotation, it is reasonable to assume that backward steps occur during the pauses waiting for ATP binding. A backward step size smaller than 36° is also consistent with the notion that the pausing positions waiting for $Na^+$ and ATP bindings are different in the $EhV_oV_1$ complex, and backward steps occur at the intermediate pausing position of $EhV_1$ between pausing positions of $EhV_o$. The forward steps just before the backward and recovery steps seemed to show two kinds of step sizes, smaller than 36° and close to 36° (Fig. 8 *B* and *D*). The backward and forward steps smaller than 36° suggest Brownian motion between the adjacent pausing positions waiting for ATP and $Na^+$ bindings. Furthermore, the 36° forward steps just before the backward steps suggest a standard forward step in $EhV_o$ followed by the Brownian backward step to the adjacent pausing position of $EhV_1$, and the 36° recovery steps after the backward steps suggest a resumption of the rotation after ATP binding to $EhV_1$.

Then, to test the hypothesis that the backward steps occur equally at three pausing positions of $EhV_1$, we prepared other mutants, isolated $EhV_1$(BR350K) and $EhV_oV_1$(BR350K). Because an arginine residue in the B subunit (BArg350) of $EhV_1$ plays a crucial role in ATP hydrolysis (*SI Appendix*, Fig. S13) (42), the rotation rate of the $EhV_1$(BR350K) mutant

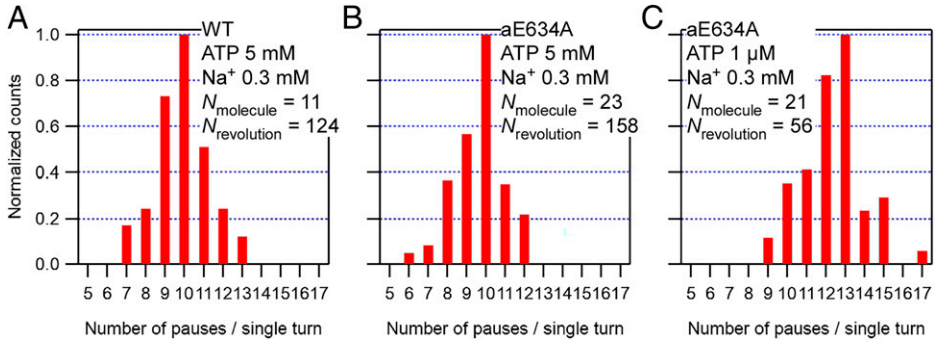


**Fig. 4.** Number of detected pauses per single turn of (*A*) wild type at 5 mM ATP and 0.3 mM $Na^+$ corresponding to Fig. 3 and *SI Appendix*, Fig. S7; (*B*) aE634A at 5 mM ATP and 0.3 mM $Na^+$ corresponding to Fig. 5 and *SI Appendix*, Fig. S8; and (*C*) aE634A at 1 μM ATP and 0.3 mM $Na^+$ corresponding to Fig. 7 and *SI Appendix*, Fig. S10.

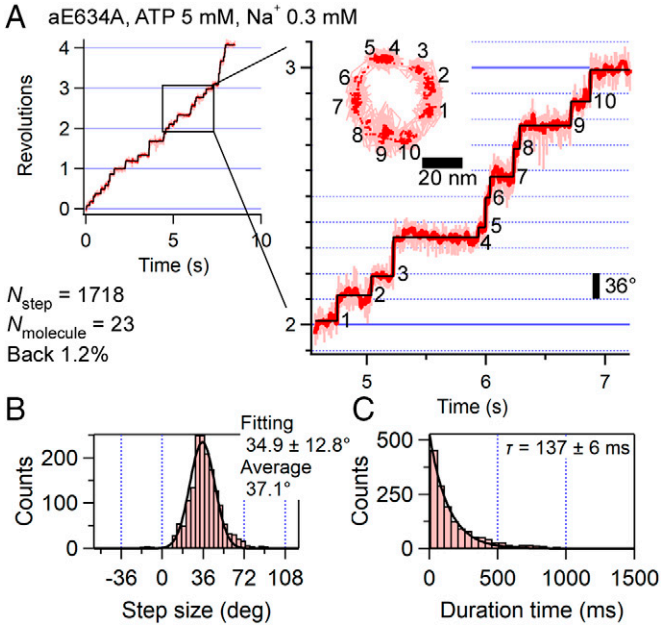


**Fig. 5.** (*A*) Typical trajectory of ATP-driven rotation of aE634A at 5 mM ATP and 0.3 mM $Na^+$ recorded at 1,000 fps (1 ms time resolution). (*Right*) Enlarged view of one revolution (360°). Pink, red, and black traces represent raw, median-filtered (current ± 7 frames), and fitted trajectories, respectively. (*Inset*) The corresponding *x*–*y* trajectory. Pink lines and red dots represent the raw and median-filtered (current ± 7 frames) coordinates, respectively. We collected 1,718 steps from 23 molecules. Other examples of trajectories are shown in *SI Appendix*, Fig. S9. (*B*) Distribution of the step size fitted with a single Gaussian assuming a single peak. The values at the top right are the fitted parameter (peak ± SD) and average. The ratio of backward steps was 1.2%. (*C*) Distribution of the duration time before the forward step fitted with a single exponential decay function. The value at the top right is the obtained time constant (fitted value ± SE of the fit).

decreases about 100 times compared to that of the wild-type $EhV_1$ (47). This property makes ATP cleavage pauses of $EhV_1$ much longer in $EhV_oV_1$(BR350K) even at high [ATP], and the pauses of $EhV_o$ and $EhV_1$ become distinguishable. The rotations of $EhV_1$(BR350K) and $EhV_oV_1$(BR350K) observed at 0.3 mM $Na^+$ and 5 mM ATP with 1,000 fps are shown in *SI Appendix*, Fig. S14. Note that in the isolated $EhV_1$(BR350K), a $His_6$ tag was introduced to the N terminus of the A subunit to immobilize the stator $A_3B_3$ ring, and a 40-nm AuNP probe was attached to the rotor D subunit (*SI Appendix*, Fig. S13). Three long pauses were observed in both mutants, attributed to ATP cleavage pauses. Similar to our previous study, $EhV_1$(BR350K) did not show clear backward steps during the long ATP cleavage pauses under this condition (*SI Appendix*, Fig. S14*A*) (47). On the other hand, $EhV_oV_1$(BR350K) exhibited frequent backward and recovery steps during the long ATP cleavage pauses (*SI Appendix*, Fig. S14*B*). The distribution of the step size showed two peaks at −11 and 11°, the sizes were smaller than 36° (*SI Appendix*, Fig. S14*C*), and these small backward and recovery steps occurred equally in all three ATP cleavage pauses of $EhV_1$.

## Discussion

**ATP-Driven Rotation of $EhV_oV_1$ Is Tightly Coupled with $Na^+$ transport.** In the present study, we directly visualized ATP-driven rotation of $EhV_oV_1$, which is rate-limited by ion transport. $EhV_oV_1$ used in this study transports $Na^+$, while most rotary ATPases transport $H^+$. This property of $EhV_oV_1$ has advantages for resolving the stepping rotation, which is rate-limited by ion transport in $V_o$. First, $H^+$ transport in rotary ATPases is thought to be achieved by a Grotthuss mechanism (15, 65) in which $H^+$ transfer is not a rate-limiting process. Indeed, the duration time of transient dwells of $F_o$ in *E. coli* $F_oF_1$ does not exhibit pH dependence ranging from pH 5 to 9, although the frequency of pause occurrence is highly affected by pH (15). In addition, changes in pH can largely affect protein stabilities and enzymatic reactions, whereas changes in [$Na^+$] would mildly affect them. Here we resolved the pauses and steps of $EhV_oV_1$ by using a mutant in which the aGlu634 residue in the stator a subunit of $EhV_o$ was substituted with alanine (aE634A) and found that the duration time before the forward steps is inversely proportional to [$Na^+$] (Fig. 6*E*). We previously confirmed that the coupling in $EhV_oV_1$ is retained by using DCCD (*N*, *N*′-dicyclohexylcarbodiimide) modification assays (17). [$Na^+$] dependency of the rotation rate in both the wild type and aE634A (Fig. 2*C*) is also strong evidence for the intact coupling. The present study demonstrates ATP-driven rotation of a rotary ATPase rate-limited by ion transport and tight coupling between ion binding and the rotational step, although single-molecule studies of ATP-driven rotation of $H^+$-transporting rotary ATPases have been reported (13–15, 66–69).

We found that both the wild type and aE634A mainly have 10 pauses per single turn and 36° steps (Figs. 3 and 5), which reflect the structural symmetry of the $c_{10}$ ring under conditions in which only $Na^+$-binding is rate-limiting for rotation (0.3 mM $Na^+$ and 5 mM ATP). In addition, numbers of pauses larger or smaller than 10 per single turn were also observed (Fig. 4). From the time constants for the elementary steps of the ATP hydrolysis

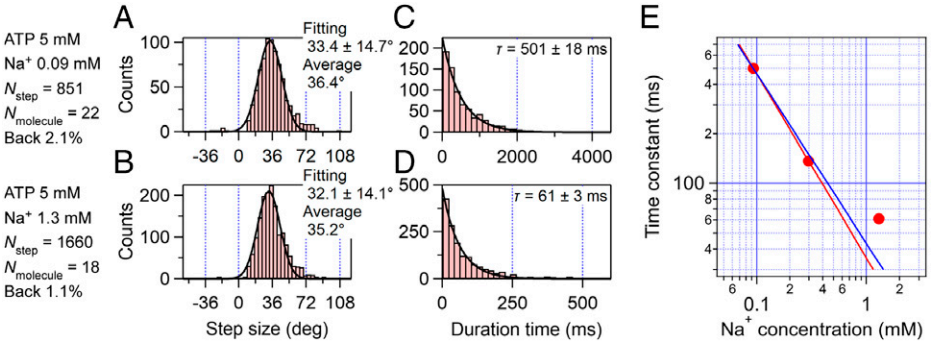


**Fig. 6.** Single-molecule analysis of aE634A at saturated [ATP] (5 mM). Experimental conditions are described on the left. Examples of trajectories are shown in *SI Appendix*, Fig. S10. (*A* and *B*) Distribution of the step size at 0.09 and 1.3 mM $Na^+$. Black lines represent fitting with single Gaussians. The values at the top right are the fitted parameters (peak ± SD) and averages. (*C* and *D*) Distribution of the duration time before the forward step. Black lines represent fitting with single exponential decay functions. The value at the top right is the obtained time constant (fitted value ± SE of the fit). (*E*) Plot between [$Na^+$] (0.09, 0.3, and 1.3 mM) and time constant obtained by the fitting at 5 mM ATP. The solid red line represents a straight line connecting two data points at 0.09 and 0.3 mM $Na^+$, and its slope is −1.1. The solid blue line is the result of linear fitting among all three data points. The obtained slope is −1.0.

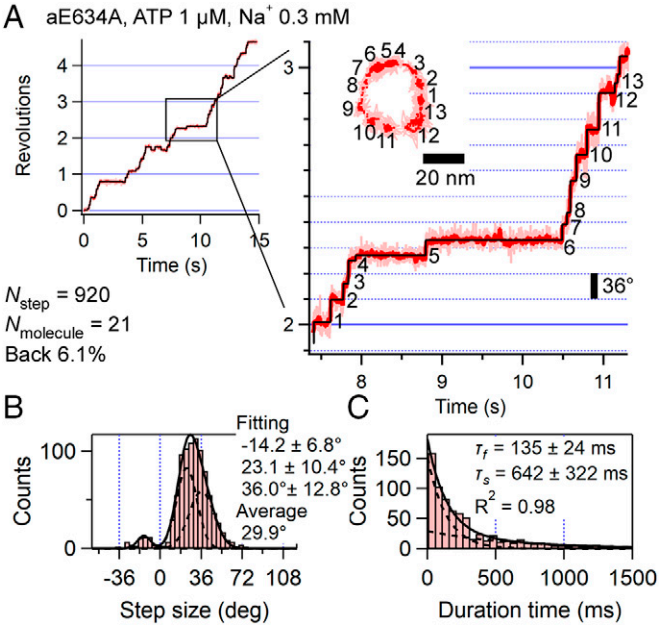


**Fig. 7.** (*A*) Typical trajectory of ATP-driven rotation of aE634A at 1 μM ATP and 0.3 mM $Na^+$ recorded at 1,000 fps (1 ms time resolution). (*Right*) Enlarged view of one revolution (360°). Pink, red, and black traces represent raw, median-filtered (current ± 7 frames), and fitted trajectories, respectively. (*Inset*) The corresponding *x*–*y* trajectory. Pink lines and red dots represent the raw and median-filtered (current ± 7 frames) coordinates, respectively. We collected 920 steps from 21 molecules. Other examples of trajectories are shown in *SI Appendix*, Fig. S11. (*B*) Distribution of the step size fitted with the sum of three Gaussians: one peak in backward (minus) direction and two peaks in forward (plus) direction, one of which was fixed at 36°, assuming that it was the step of $EhV_o$. The ratio of backward steps was 6.1%. (*C*) Distribution of the duration time before the forward step fitted with the sum of two exponential decay functions. The values at the top right are obtained time constants (fitted value ± SE of the fit) and the coefficient of determination ($R^2$) of fitting.

reaction in $EhV_1$ and the time resolution of measurement (0.33 and 1 ms for the wild type and aE634A, respectively), we can consider the case where more than 10 pauses are detected (Fig. 4). From the $k_{on}^{ATP}$ of the wild type and aE634A ($2.0 \times 10^6$ and $2.1 \times 10^6$ $M^{-1}$ $s^{-1}$, respectively; Table 1), the time constants for ATP binding are estimated to be about 0.1 ms at 5 mM ATP. In addition, by using isolated $EhV_1$, we previously reported that the time constants for ATP cleavage and phosphate release are smaller than 1 ms, and that for ADP release is 2.5 ms. Furthermore, ADP release occurs at a different angle from that of ATP binding, while ATP cleavage and phosphate release occur at the same angle as ATP binding (47). Considering the stochastic nature of the pause duration and current time resolution, these elementary events, especially ADP release, can be also detected. If the time resolution and the localization precision are further improved, detection of 16 pauses (10, 3, and 3 pauses for $Na^+$ binding, ATP binding, and ADP release, respectively) would become possible and give us further insight into the energy transduction mechanism of the $EhV_oV_1$ complex. Similarly, a number of pauses fewer than 10 can also occur stochastically due to $Na^+$ binding events with shorter duration times than the time resolution. Another possible explanation is stochastic $H^+$ transport instead of $Na^+$ in $EhV_oV_1$ at low [$Na^+$]. It has been reported that $H^+$ can bind to the ion-binding site of the $EhV_o$ c subunit when [$Na^+$] is sufficiently low (44). Because $H^+$ binding will not be the rate-limiting factor as described above, the pauses could not be detected at the current time resolution (14). In the present study, we could not distinguish $Na^+$ and $H^+$ bindings and assumed that steps are triggered by $Na^+$ bindings. Whether or not $EhV_oV_1$ really transports $H^+$ under low-[$Na^+$] conditions will be addressed elsewhere. Furthermore, we need to mention that the step-finding algorithm we used cannot perfectly eliminate overfittings and underfittings (62, 64). Due to these experimental and analytical limitations, we cannot confidently identify which dwells correspond to $EhV_1$ or $EhV_o$.

The $V_{max}^{ATP}$ of the wild-type $EhV_oV_1$ (40.0 ± 0.3 rps) at 300 mM $Na^+$ was smaller than that of the isolated $EhV_1$ (117 ± 3 rps) (Fig. 2*B* and Table 1) (47). The difference is presumably caused by the elementary steps of $Na^+$ transport in $EhV_o$, especially by $Na^+$ release, and/or the interaction (molecular friction) between the rotor $c_{10}$ ring and stator a subunit. If we assume that $Na^+$ release is rate-limiting, we can estimate the time constant for $Na^+$ release to be 1.6 ms from the difference of the $V_{max}^{ATP}$ between $EhV_oV_1$ and $EhV_1$. Note that in the present study, both entry and exit half-channels of the a subunit were exposed to the solution with 300 mM $Na^+$ because we used detergent-solubilized $EhV_oV_1$. The effect of $Na^+$ rebinding from the exit half-channel on the rotation rate of $EhV_oV_1$ is an interesting question that needs to be clarified. On the other hand, the $V_{max}^{ATP}$ of aE634A (4.58 ± 0.04 rps) at 300 mM $Na^+$ was approximately one-tenth that of the wild type (40.0 ± 0.3 rps) (Fig. 2*B* and Table 1). Michaelis–Menten kinetics analysis showed that the $k_{on}^{ATP}$ of aE634A was similar to that of the wild type, although the $k_{on}^{Na}$ of aE634A was

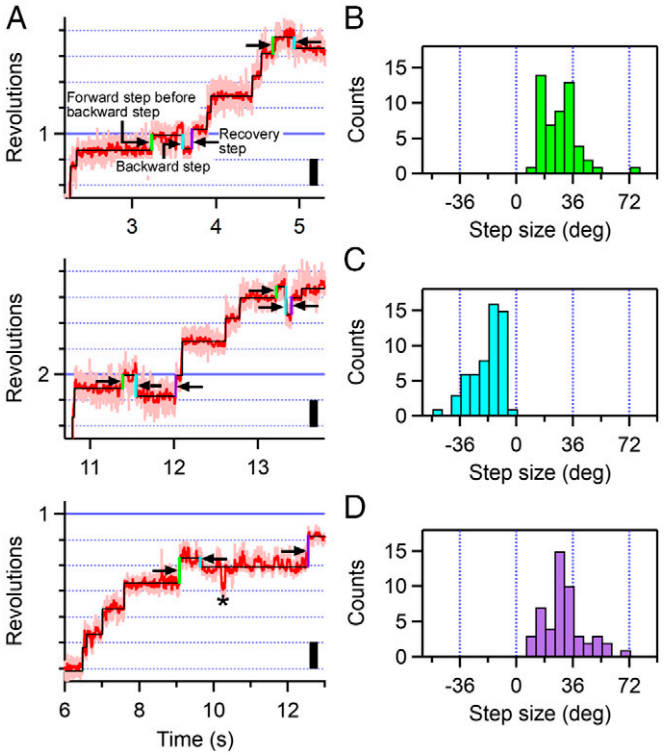


**Fig. 8.** Backward steps of aE634A observed at 1 μM ATP and 0.3 mM $Na^+$ with 1,000 fps (1 ms time resolution). (*A*) Examples of trajectories showing the backward steps. The pink, red, and black traces represent the raw, median-filtered (current ± 7 frames), and fitted trajectories of the median-filtered data identified by the algorithm, respectively. The green, cyan, and purple lines indicate forward steps just before backward steps, backward steps, and forward steps just after backward steps (recovery steps), respectively. An asterisk indicates a backward step that is not detected as a step by the algorithm (underfitting). (*B*–*D*) Distributions of step size for forward steps just before backward steps, backward steps, and recovery steps, respectively. In *B* and *D*, the distributions seemed to show two peaks at <36° and 36°. In *C*, the peak position was larger than −36°, and the average value was −18.8°.

significantly decreased compared with that of the wild type (Tables 1 and 2). These results indicate that the aE634A mutation has little effect on ATP binding to $EhV_1$. The mutated glutamate residue is located on the surface of entry half-channel of the a subunit (Fig. 1*C*), and the decrease in $k_{on}^{Na}$ is likely caused by the loss of a negative charge. Interestingly, this glutamate residue is completely conserved among $Na^+$- and $H^+$-transporting V-ATPases (*SI Appendix*, Figs. S1 and S2) (24, 26, 70, 71). Therefore, it may have a common role in efficient ion uptake for both $Na^+$ and $H^+$. Consistent with this notion, ion selectivity seems to be determined by the ion-binding site of the c ring rather than the half-channels in the a subunit (72, 73).

The rotation rate of both the wild type and aE634A showed a biphasic response to $[Na^+]$ (Fig. 2*C* and Table 2). This biphasic response was also reported previously for the ATPase activity of detergent-solubilized $EhV_oV_1$ (17, 61). The Michaelis–Menten parameters obtained in this study are slightly different from those in previous studies, presumably due to differences in experimental conditions, especially pH and $[Na^+]$ contaminating the observation buffer. Regarding the $Na^+$ contamination in the experimental system, it should be noted that it is difficult to determine affinity at the submicromolar range since the observation buffer contains at least 90 μM $Na^+$ (*SI Appendix*, Fig. S6). The biphasic response to $[Na^+]$ strongly suggests two different $Na^+$-binding sites of $EhV_oV_1$ with largely different affinities. One possible explanation is that these sites are related to the entry and exit half-channels of the a subunit. The high-affinity binding site may correspond to $Na^+$ binding to the c ring from the entry site because the dissociation constant of $Na^+$ to the c subunit in the $EhV_oV_1$ complex has been reported as 12 μM in the absence of ATP (44). On the other hand, the low-affinity $Na^+$ binding site corresponding to $K_{m2}^{Na}$ has not been identified yet. We assume that the low-affinity site would be physiologically important because the intracellular $[Na^+]$ in *E. hirae* has been reported to be several tens of millimolar (38, 41, 74). To clarify the mechanism of the biphasic response of $EhV_oV_1$ to $[Na^+]$, it will be required to embed $EhV_oV_1$ in the lipid membrane and change the $[Na^+]$ in the entry and exit sides independently (75). Alternatively, mutagenesis in the $Na^+$ exit half-channel of the a subunit will provide insights into the biphasic response. Recently, Yanagisawa and Frasch (15) investigated *E. coli* $F_oF_1$ mutants by replacing charged or polar residues in the entry and exit half-channels with nonpolar leucine residues and successfully revealed that these residues possess optimal $pK_a$ values for unidirectional $H^+$ transfer. A similar approach would be also helpful for $EhV_oV_1$.

**Rigid Component in Coupling between $EhV_o$ and $EhV_1$ in the $EhV_oV_1$ Complex.** By using single-molecule imaging of aE634A under conditions where both $Na^+$ and ATP bindings are rate-limiting for rotation, we visualized the pauses of $EhV_o$ and $EhV_1$ simultaneously. We found that aE634A mainly shows 13 pauses per single turn under this condition (Figs. 4*C* and 7*A* and *SI Appendix*, Fig. S10). Furthermore, occasional backward and recovery steps smaller than 36° were observed (Fig. 8), not only in aE634A but also during the three long ATP cleavage pauses of $EhV_oV_1$(BR350K) (*SI Appendix*, Fig. S14). These results indicate that the pausing positions waiting for $Na^+$ and ATP bindings are different, and transitions occur between adjacent pausing positions of $EhV_o$ and $EhV_1$. These results also indicate that the ATP hydrolysis reaction in $EhV_1$ is tightly coupled with $Na^+$ transport in $EhV_o$, and this coupling has a rigid component. Considering our observation system where the c ring of $EhV_o$ is immobilized on the glass surface and the AuNP probe is attached to the A subunit of $EhV_1$ (Fig. 2*A*), if the complex shows a fully elastic coupling, the pausing positions of $EhV_o$ and $EhV_1$ would be superimposed by deformation of the peripheral $E_2G_2$ stalks or the central DF shaft. In this case, a single turn (360° revolution) would be divided into two 108° (36° × 3) and one 144° (36° × 4) rotations with extensive deformation. However, our results clearly showed 10 pauses per single turn (36° step) at high [ATP] and 13 pauses at low [ATP], suggesting rigid coupling in which the 120° steps in $EhV_1$ are retained in the presence of a structural symmetry mismatch between $EhV_o$ and $EhV_1$. However, we should mention that with our observation system, even if elastic deformation of the peripheral stalks causes the motion of the a subunit of $EhV_o$ to move to forward or backward $Na^+$ binding angle during the pause of $EhV_1$ waiting for ATP binding, it cannot be detected as a step because we attached the AuNP probe to the A subunit of $EhV_1$. Therefore, the present results do not completely rule out the possibility of elastic deformation in $EhV_oV_1$ (*SI Appendix*, Fig. S15).

Different pausing positions between $V_o$ and $V_1$ have also been reported by a single-molecule study of detergent-solubilized $H^+$-transporting *Thermus thermophilus* V/A-ATPase, which acts as an ATP synthase (20). Here we denote this enzyme as $TtV_oV_1$ following previous studies (20, 24), although it is believed to have been introduced by horizontal gene transfer from a habitat sharing archaea (8). During rotation in the ATP hydrolysis direction, $TtV_oV_1$ showed 30° steps derived from the $c_{12}$ ring of $TtV_o$ and extra pauses between two adjacent pauses of $TtV_o$. These extra pauses were attributed to catalytic dwells of $TtV_1$. Furthermore, corresponding structures were also recently revealed by a cryo-EM study of nanodisc-embedded $TtV_oV_1$ (24). Zhou and Sazanov (24) resolved the structures of two substates in addition to three main states, which reflect the threefold structural symmetry of $TtV_1$. Those substates, 1L and 1R, which differ in the relative positions of $TtV_o$ and $TtV_1$, exhibited a slight twist of the central shaft and deformation of the peripheral stalks against state 1. It remains uncertain which pauses found in the single-molecule study correspond to those substates. It is intriguing that the angles of $TtV_o$ and $TtV_1$ do not coincide although $TtV_o$ has a $c_{12}$ ring and no symmetry mismatch with $TtV_1$.

The rigid component in $EhV_oV_1$ coupling is distinct from *E. coli*, *Bacillus* PS3, and yeast mitochondrial F-ATPases, in which cryo-EM studies have indicated an elastic coupling (25, 29, 35). These F-ATPases have $c_{10}$ rings (34, 76) and the same structural symmetry mismatches as $EhV_oV_1$. Structural analysis of *E. coli* or *Bacillus* PS3 $F_oF_1$ has revealed three rotational steps that are classified into two 108° steps and one 144° step. This significant mismatch is tolerated by the flexible peripheral stalk rather than the central shaft (25, 29, 77). Actually, a very recent cryo-EM study of yeast mitochondrial $F_oF_1$ revealed extensive deformation of the peripheral stalk during catalysis (35). In rotary ATPases, the number of peripheral stalks varies from one to three, depending on the enzymes (6, 78, 79). *E. coli*, *Bacillus* PS3, and yeast $F_oF_1$ possess only one peripheral stalk (25, 29), whereas $EhV_oV_1$ has two peripheral stalks that can strongly connect two motor domains (Fig. 1*A*) (26). As a result, $EhV_oV_1$ would rotate rigidly without large, elastic deformations. Consistent with this notion, a cryo-EM study of yeast $V_oV_1$, which has three peripheral stalks, showed three almost uniform 120° steps despite having a $c_{10}$ ring (27), although the possibility of uniform steps due to asymmetry in the c ring of yeast $V_oV_1$ should be considered as proposed by the author.

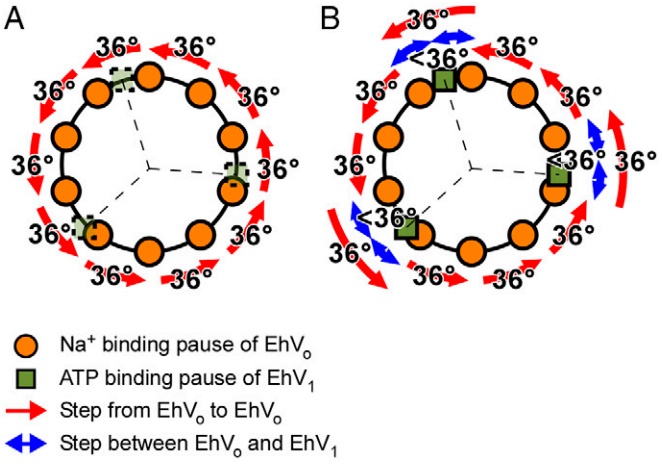


**Fig. 9.** Schematic models of the stepping rotation and rigid coupling of $EhV_oV_1$. The orange circles and dark green squares indicate the pausing positions waiting for $Na^+$ binding to $EhV_o$ and ATP binding to $EhV_1$, respectively. The red arrows indicate the 36° steps between adjacent pausing positions for the $EhV_o$. The blue arrows indicate the backward and forward steps smaller than 36° between adjacent pausing positions for $EhV_o$ and $EhV_1$. (*A*) Condition in which only $Na^+$ binding to $EhV_o$ is rate-limiting. In this condition, the pauses waiting for ATP binding to $EhV_1$ are too short to be detected, and $EhV_oV_1$ rotates unidirectionally without backward steps. (*B*) Condition in which both $Na^+$ and ATP bindings are rate-limiting. The pausing positions waiting for ATP binding are visualized, and then 13 pausing positions are detected per single turn. Because no torque is generated during the pauses waiting for ATP binding to $EhV_1$, $EhV_oV_1$ rotates to the backward and forward pausing positions of $EhV_o$ driven by Brownian motion. As a result, backward and forward steps smaller than 36° are observed. A detailed model is shown in *SI Appendix*, Fig. S15.

In addition to the number of peripheral stalks, the number of c subunits in the rotor ring also varies widely from 8 to 17 among species (58, 59). This makes the issue more complicated because a different number of c subunits will change the step size and the ion-to-ATP ratio. Furthermore, the number of transmembrane helices in a c subunit monomer also differs among species. For example, although both $EhV_oV_1$ and *E. coli* $F_oF_1$ have $c_{10}$ rings, each c subunit consists of tetratransmembrane and double-transmembrane helices, respectively (25, 55). This results in largely different diameters of the $c_{10}$ ring, 8 and 5 nm for $EhV_oV_1$ and *E. coli* $F_oF_1$, respectively (26). Obviously, larger rings would require larger deformations to adjust the relative angles between $V_o/F_o$ and $V_1/F_1$ if elastic coupling is assumed. Another interesting feature of $EhV_oV_1$ with the large c ring is its off-axis rotation, which may affect the coupling between $EhV_o$ and $EhV_1$ (26). However, the off-axis rotation was not resolved in the present single-molecule experiments. To understand the common and diverse mechanisms of energy transduction in rotary ATPases, a comprehensive study of various ATPases with rotor c rings of different c subunit numbers and sizes will be required.

**Brownian Ratchet Rotation of $EhV_o$.** Fig. 9 shows a schematic model of the stepping rotation of $EhV_oV_1$ at high [ATP] and low [$Na^+$] (Fig. 9*A*) and at low [ATP] and low [$Na^+$] (Fig. 9*B*). In the present study, backward steps were rarely observed when [ATP] is high (5 mM) in both the wild type and aE634A (Figs. 3*B*, 5*B*, and 6 *A* and *B*). In $EhV_oV_1$, the torque for ATP-driven rotation is generated by ATP binding and ADP release in $EhV_1$ (47), and the value has been estimated to be 20 pNnm (17). When [ATP] is high, time constants for ATP binding and ADP release are both small, and the torque from $EhV_1$ will be applied to $EhV_o$ almost constantly. Therefore, $EhV_oV_1$ will show unidirectional rotation without backward steps (Fig. 9*A*). On the other hand, when [ATP] is low (1 μM) and where the time constant for ATP binding is large (476 or 642 ms; Table 1 and Fig. 7*C*), backward steps were observed occasionally (Fig. 8*A*). The size of the backward steps was much smaller than 36° (14.2 or 18.8°; Figs. 7*B* and 8*C*). Because no torque is applied when $EhV_oV_1$ is waiting for ATP binding at the pausing position of $EhV_1$ (Fig. 9*B*, dark green), it can move to the adjacent backward (and also forward) pausing position of $EhV_o$ by Brownian motion (Fig. 9*B*, blue arrows). Backward and recovery steps smaller than 36° were more frequently observed in $EhV_oV_1$(BR350K), in which ATP cleavage pauses are prominently longer than in the wild type (*SI Appendix*, Fig. S14). Importantly, backward steps occurred equally during the three ATP cleavage pauses of $EhV_1$, consistent with the notion that backward steps are driven by thermal fluctuation, not by elastic strain accumulation. These results support a Brownian ratchet model of $EhV_o$ rotation in addition to the rigid coupling component of $EhV_oV_1$. However, it should be noted that the elastic deformations at the transitions between $EhV_1$ and $EhV_o$ pausing angles cannot be detected by the current observation system (*SI Appendix*, Fig. S15). Also, note that the size of backward steps occurring at the three pausing positions of $EhV_1$ will not be uniform in the model shown in Fig. 9*B*. However, it was difficult for us to resolve any difference under the current experimental setup.

In our previous study using isolated $EhV_1$, no backward steps were observed in ATP-driven rotation except under extreme experimental conditions (47). Therefore, backward and forward steps smaller than 36° observed in $EhV_oV_1$ are caused by $EhV_o$ and are presumably coupled with $Na^+$ binding/release to/from the c subunit through the two half-channels of the a subunit. A recent single-molecule study observed similar small backward steps of 11° in *E. coli* $F_oF_1$ during ATP-driven rotation and successfully revealed that backward steps are related to $H^+$ translocation between the c ring and half-channels of the a subunit (15). In a study of *E. coli* $F_oF_1$, the small backward step was attributed to the fact that *E. coli* $F_oF_1$ functions as an ATP synthase. In the case of $EhV_oV_1$, because backward steps of 36° or larger than 36° rarely occur, the backward flow of $Na^+$ seems to be suppressed. The detailed mechanisms of the backward step may be different by ATP synthesis capacity, size of the c ring, and ion species being transported. In the present study, however, the electrochemical potential of $Na^+$ could not be applied because detergent-solubilized $EhV_oV_1$ was used. To address the question of whether the electrochemical potential of $Na^+$ can drive the rotation of $EhV_oV_1$ in the opposite direction and synthesize ATP, our next projects will be single-molecule imaging and biochemical assays of $EhV_oV_1$ embedded in a lipid membrane.

## Materials and Methods

**Sample Preparation.** The construction of the expression plasmid for the wild-type $EhV_oV_1$ (pTR19-$EhV_oV_1$) was reported previously (17). For the plasmid construction of aE634A, $EhV_oV_1$(BR350K), and $EhV_1$(BR350K), PCR-based site-directed mutagenesis was performed by KOD one PCR Master Mix (Toyobo) with pTR19-$EhV_oV_1$ as a template. For expression and purification of the wild type, aE634A, $EhV_oV_1$(BR350K), and $EhV_1$(BR350K), the procedures described in our previous study were used with some modifications (17, 47). Details are described in *SI Appendix*.

**Single-Molecule Imaging.** AuNPs with a diameter of 40 nm (EMGC40, BBI) were biotinylated with biotin-alkane-thiol (HS-C11-EG3, Surfmods) and coated by streptavidin (PRO791, PROSPEC) as described in previous reports (47, 80). We followed the setting of a total internal reflection dark-field microscope system based on a high-speed complementary metal oxide semiconductor (CMOS) camera and an inverted microscope as described in our previous studies with some modifications (47). Details are described in *SI Appendix*.

**ICP-OES Measurement.** To estimate the concentrations of contaminating $Na^+$ in the observation buffers, we measured emission spectra using an ICP-OES (5100 ICP-OES, Agilent Technologies). The emission signal at $\lambda = 589.592$ nm was used for analysis. The flow rates of the plasma and assist gas (Ar) were 14 and 1.2 L/min, respectively. The standard addition method was used to avoid physical and ionization interferences. Namely, a sodium standard solution (FUJIFILM Wako) was added to the observation buffers in a range of 0.1 to 10 mg/L (4.3 to 430 μM) as a final concentration of $Na^+$. The calibration curve was extrapolated, and the absolute value of the X intercept was taken as the concentration of contaminating $Na^+$.

**Data, Materials, and Software Availability.** All study data are included in the article and/or *SI Appendix*.

**ACKNOWLEDGMENTS.** We thank Monique Honsa for advice about data analysis; Kazuyoshi Murata, Chihong Song, and Raymond N. Burton-Smith for providing us with the structural data and for their fruitful discussions; Yayoi Kon for her technical support; and all laboratory members for helpful discussions and technical advice. This work was supported by Grants-in-Aid for Scientific Research on Innovative Areas "Molecular Engine" (JP19H05380 to H.U., JP18H05425 to T.M., and JP18H05424 to R.I.); Grants-in-Aid for Scientific Research (JP21H02454 to R.I. and JP21K15060 and JP20J01316 to A.O.) from the Ministry of Education, Culture, Sports, Science, and Technology of Japan; and the National Institutes of Natural Sciences (NINS) program for cross-disciplinary study (Grant 01312001 to A.O.). A part of this work was performed with the aid of the Instrument Center of the Institute for Molecular Science.

Author affiliations: [a]Institute for Molecular Science, National Institutes of Natural Sciences, Okazaki 444-8787, Japan; [b]Department of Functional Molecular Science, School of Physical Sciences, Graduate University for Advanced Studies, Hayama 240-0193, Japan; [c]Department of Applied Chemistry, Graduate School of Engineering, The University of Tokyo, Tokyo 113-8656, Japan; and [d]Department of Chemistry, Graduate School of Science, Chiba University, Chiba 263-8522, Japan

1. R. Yasuda, H. Noji, M. Yoshida, K. Kinosita Jr., H. Itoh, Resolution of distinct rotational substeps by submillisecond kinetic analysis of $F_1$-ATPase. *Nature* **410**, 898–904 (2001).
2. M. Forgac, Vacuolar ATPases: Rotary proton pumps in physiology and pathophysiology. *Nat. Rev. Mol. Cell Biol.* **8**, 917–929 (2007).
3. J. E. Walker, The ATP synthase: The understood, the uncertain and the unknown. *Biochem. Soc. Trans.* **41**, 1–16 (2013).
4. P. D. Boyer, The ATP synthase–A splendid molecular machine. *Annu. Rev. Biochem.* **66**, 717–749 (1997).
5. T. Vasanthakumar, J. L. Rubinstein, Structure and roles of V-type ATPases. *Trends Biochem. Sci.* **45**, 295–307 (2020).
6. A. G. Stewart, M. Sobti, R. P. Harvey, D. Stock, Rotary ATPases: Models, machine elements and technical specifications. *Bioarchitecture* **3**, 2–12 (2013).
7. G. Grüber, M. S. S. Manimekalai, F. Mayer, V. Müller, ATP synthases from archaea: The beauty of a molecular motor. *Biochim. Biophys. Acta* **1837**, 940–952 (2014).
8. J. P. Gogarten *et al.*, Evolution of the vacuolar $H^+$-ATPase: Implications for the origin of eukaryotes. *Proc. Natl. Acad. Sci. U.S.A.* **86**, 6661–6665 (1989).
9. H. Sielaff *et al.*, Domain compliance and elastic power transmission in rotary $F_{(O)}F_{(1)}$-ATPase. *Proc. Natl. Acad. Sci. U.S.A.* **105**, 17760–17765 (2008).
10. H. Sielaff, H. Rennekamp, S. Engelbrecht, W. Junge, Functional halt positions of rotary $F_OF_1$-ATPase correlated with crystal structures. *Biophys. J.* **95**, 4979–4987 (2008).
11. R. Yasuda, H. Noji, K. Kinosita Jr., M. Yoshida, $F_1$-ATPase is a highly efficient molecular motor that rotates with discrete 120° steps. *Cell* **93**, 1117–1124 (1998).
12. H. Noji, R. Yasuda, M. Yoshida, K. Kinosita Jr., Direct observation of the rotation of $F_1$-ATPase. *Nature* **386**, 299–302 (1997).
13. R. Ishmukhametov, T. Hornung, D. Spetzler, W. D. Frasch, Direct observation of stepped proteolipid ring rotation in *E. coli* $F_OF_1$-ATP synthase. *EMBO J.* **29**, 3911–3923 (2010).
14. S. Yanagisawa, W. D. Frasch, Protonation-dependent stepped rotation of the F-type ATP synthase c-ring observed by single-molecule measurements. *J. Biol. Chem.* **292**, 17093–17100 (2017).
15. S. Yanagisawa, W. D. Frasch, pH-dependent 11° $F_1F_O$ ATP synthase sub-steps reveal insight into the $F_O$ torque generating mechanism. *eLife* **10**, e70016 (2021).
16. H. Sielaff, S. Yanagisawa, W. D. Frasch, W. Junge, M. Börsch, Structural asymmetry and kinetic limping of single rotary F-ATP synthases. *Molecules* **24**, 504 (2019).
17. H. Ueno *et al.*, Torque generation of *Enterococcus hirae* V-ATPase. *J. Biol. Chem.* **289**, 31212–31223 (2014).
18. J. Martin, J. Hudson, T. Hornung, W. D. Frasch, $F_o$-driven rotation in the ATP synthase direction against the force of $F_1$ ATPase in the $F_oF_1$ ATP synthase. *J. Biol. Chem.* **290**, 10717–10728 (2015).
19. J. L. Martin, R. Ishmukhametov, T. Hornung, Z. Ahmad, W. D. Frasch, Anatomy of $F_1$-ATPase powered rotation. *Proc. Natl. Acad. Sci. U.S.A.* **111**, 3715–3720 (2014).
20. S. Furuike *et al.*, Resolving stepping rotation in Thermus thermophilus $H(^+)$-ATPase/synthase with an essentially drag-free probe. *Nat. Commun.* **2**, 233 (2011).
21. W. C. Y. Lau, J. L. Rubinstein, Structure of intact *Thermus thermophilus* V-ATPase by cryo-EM reveals organization of the membrane-bound $V_{(O)}$ motor. *Proc. Natl. Acad. Sci. U.S.A.* **107**, 1367–1372 (2010).
22. M. G. Düser *et al.*, 36° step size of proton-driven *c*-ring rotation in $F_oF_1$-ATP synthase. *EMBO J.* **28**, 2689–2696 (2009).
23. B. Zimmermann, M. Diez, N. Zarrabi, P. Gräber, M. Börsch, Movements of the epsilon-subunit during catalysis and activation in single membrane-bound H(+)-ATP synthase. *EMBO J.* **24**, 2053–2063 (2005).
24. L. Zhou, L. A. Sazanov, Structure and conformational plasticity of the intact *Thermus thermophilus* V/A-type ATPase. *Science* **365**, eaaw9144 (2019).
25. M. Sobti *et al.*, Cryo-EM structures provide insight into how *E. coli* $F_1F_o$ ATP synthase accommodates symmetry mismatch. *Nat. Commun.* **11**, 2615 (2020).
26. J. Tsunoda *et al.*, Off-axis rotor in *Enterococcus hirae* V-ATPase visualized by Zernike phase plate single-particle cryo-electron microscopy. *Sci. Rep.* **8**, 15632 (2018).
27. M. M. Khan *et al.*, Oxidative stress protein Oxr1 promotes V-ATPase holoenzyme disassembly in catalytic activity-independent manner. *EMBO J.* **41**, e109360 (2022).
28. J. Kishikawa *et al.*, Structural snapshots of V/A-ATPase reveal the rotary catalytic mechanism of rotary ATPases. *Nat. Commun.* **13**, 1213 (2022).
29. H. Guo, T. Suzuki, J. L. Rubinstein, Structure of a bacterial ATP synthase. *eLife* **8**, e43128 (2019).
30. A. Zhou *et al.*, Structure and conformational states of the bovine mitochondrial ATP synthase by cryo-EM. *eLife* **4**, e10180 (2015).
31. S.-H. Roh *et al.*, The 3.5-Å CryoEM structure of nanodisc-reconstituted yeast vacuolar ATPase $V_o$ proton channel. *Mol. Cell* **69**, 993–1004.e3 (2018).
32. S.-H. Roh *et al.*, Cryo-EM and MD infer water-mediated proton transport and autoinhibition mechanisms of $V_o$ complex. *Sci. Adv.* **6**, eabb9605 (2020).
33. Y. M. Abbas, D. Wu, S. A. Bueler, C. V. Robinson, J. L. Rubinstein, Structure of V-ATPase from the mammalian brain. *Science* **367**, 1240–1246 (2020).
34. B. J. Murphy *et al.*, Rotary substates of mitochondrial ATP synthase reveal the basis of flexible $F_1$-$F_o$ coupling. *Science* **364**, eaaw9128 (2019).
35. H. Guo, J. L. Rubinstein, Structure of ATP synthase under strain during catalysis. *Nat. Commun.* **13**, 2232 (2022). Correction in: *Nat Commun.* **13**, 2849 (2022).
36. A. Waterhouse *et al.*, SWISS-MODEL: Homology modelling of protein structures and complexes. *Nucleic Acids Res.* **46**, W296–W303 (2018).
37. D. L. Heefner, F. M. Harold, ATP-driven sodium pump in *Streptococcus faecalis*. *Proc. Natl. Acad. Sci. U.S.A.* **79**, 2798–2802 (1982).
38. M. Ikegami, H. Takahashi, K. Igarashi, Y. Kakinuma, Sodium ATPase and sodium/proton antiporter are not obligatory for sodium homeostasis of *Enterococcus hirae* at acid pH. *Biosci. Biotechnol. Biochem.* **64**, 1088–1092 (2000).
39. Y. Kakinuma, I. Yamato, T. Murata, Structure and function of vacuolar $Na^+$-translocating ATPase in *Enterococcus hirae*. *J. Bioenerg. Biomembr.* **31**, 7–14 (1999).
40. Y. Kakinuma, K. Igarashi, Electrogenic $Na^+$ transport by *Enterococcus hirae* $Na(^+)$-ATPase. *FEBS Lett.* **359**, 255–258 (1995).
41. Y. Kakinuma, K. Igarashi, Amplification of the $Na^+$-ATPase of *Streptococcus faecalis* at alkaline pH. *FEBS Lett.* **261**, 135–138 (1990).
42. S. Arai *et al.*, Rotation mechanism of *Enterococcus hirae* $V_1$-ATPase based on asymmetric crystal structures. *Nature* **493**, 703–707 (2013).
43. K. Suzuki *et al.*, Crystal structures of the ATP-binding and ADP-release dwells of the $V_1$ rotary motor. *Nat. Commun.* **7**, 13235 (2016).
44. T. Murata *et al.*, Ion binding and selectivity of the rotor ring of the $Na^+$-transporting V-ATPase. *Proc. Natl. Acad. Sci. U.S.A.* **105**, 8607–8612 (2008).
45. H. Imamura *et al.*, Evidence for rotation of $V_1$-ATPase. *Proc. Natl. Acad. Sci. U.S.A.* **100**, 2312–2315 (2003).
46. Y. Minagawa *et al.*, Basic properties of rotary dynamics of the molecular motor *Enterococcus hirae* $V_1$-ATPase. *J. Biol. Chem.* **288**, 32700–32707 (2013).
47. T. Iida *et al.*, Single-molecule analysis reveals rotational substeps and chemo-mechanical coupling scheme of *Enterococcus hirae* $V_1$-ATPase. *J. Biol. Chem.* **294**, 17017–17030 (2019).
48. M. Allegretti *et al.*, Horizontal membrane-intrinsic α-helices in the stator *a*-subunit of an F-type ATP synthase. *Nature* **521**, 237–240 (2015).
49. A. Hahn, J. Vonck, D. J. Mills, T. Meier, W. Kühlbrandt, Structure, mechanism, and regulation of the chloroplast ATP synthase. *Science* **360**, eaat4318 (2018).
50. C. M. Angevine, K. A. G. Herold, O. D. Vincent, R. H. Fillingame, Aqueous access pathways in ATP synthase subunit a. Reactivity of cysteine substituted into transmembrane helices 1, 3, and 5. *J. Biol. Chem.* **282**, 9001–9007 (2007).
51. W. Junge, ATP synthase and other motor proteins. *Proc. Natl. Acad. Sci. U.S.A.* **96**, 4735–4737 (1999).
52. S. B. Vik, B. J. Antonio, A mechanism of proton translocation by $F_1F_0$ ATP synthases suggested by double mutants of the *a* subunit. *J. Biol. Chem.* **269**, 30364–30369 (1994).
53. W. Junge, H. Lill, S. Engelbrecht, ATP synthase: An electrochemical transducer with rotatory mechanics. *Trends Biochem. Sci.* **22**, 420–423 (1997).
54. C. von Ballmoos, P. Dimroth, Two distinct proton binding sites in the ATP synthase family. *Biochemistry* **46**, 11800–11809 (2007).
55. T. Murata, I. Yamato, Y. Kakinuma, A. G. W. Leslie, J. E. Walker, Structure of the rotor of the V-Type $Na^+$-ATPase from *Enterococcus hirae*. *Science* **308**, 654–659 (2005).
56. C. Bai, A. Warshel, Revisiting the protomotive vectorial motion of $F_0$-ATPase. *Proc. Natl. Acad. Sci. U.S.A.* **116**, 19484–19489 (2019).
57. D. Matthies *et al.*, High-resolution structure and mechanism of an F/V-hybrid rotor ring in a $Na^+$-coupled ATP synthase. *Nat. Commun.* **5**, 5286 (2014).
58. H. Noji, H. Ueno, R. Kobayashi, Correlation between the numbers of rotation steps in the ATPase and proton-conducting domains of F- and V-ATPases. *Biophys. Rev.* **12**, 303–307 (2020).
59. A. Cheuk, T. Meier, Rotor subunits adaptations in ATP synthases from photosynthetic organisms. *Biochem. Soc. Trans.* **49**, 541–550 (2021).
60. W. Junge, H. Sielaff, S. Engelbrecht, Torque generation and elastic power transmission in the rotary $F_{(O)}F_{(1)}$-ATPase. *Nature* **459**, 364–370 (2009).
61. T. Murata, K. Takase, I. Yamato, K. Igarashi, Y. Kakinuma, Properties of the V0V1 $Na^+$-ATPase from *Enterococcus hirae* and its V0 moiety. *J. Biochem.* **125**, 414–421 (1999).
62. J. W. J. Kerssemakers *et al.*, Assembly dynamics of microtubules at molecular resolution. *Nature* **442**, 709–712 (2006).
63. J. Ando *et al.*, Small stepping motion of processive dynein revealed by load-free high-speed single-particle tracking. *Sci. Rep.* **10**, 1080 (2020).
64. A. Nakamura, K.-I. Okazaki, T. Furuta, M. Sakurai, R. Iino, Processive chitinase is Brownian monorail operated by fast catalysis after peeling rail from crystalline chitin. *Nat. Commun.* **9**, 3814 (2018).

65. T. E. Spikes, M. G. Montgomery, J. E. Walker, Structure of the dimeric ATP synthase from bovine mitochondria. *Proc. Natl. Acad. Sci. U.S.A.* **117**, 23519–23526 (2020).
66. K. Nishio, A. Iwamoto-Kihara, A. Yamamoto, Y. Wada, M. Futai, Subunit rotation of ATP synthase embedded in membranes: *a* or β Subunit rotation relative to the *c* subunit ring. *Proc. Natl. Acad. Sci. U.S.A.* **99**, 13448–13452 (2002).
67. H. Ueno, T. Suzuki, K. Kinosita Jr., M. Yoshida, ATP-driven stepwise rotation of $F_oF_1$-ATP synthase. *Proc. Natl. Acad. Sci. U.S.A.* **102**, 1333–1338 (2005).
68. K. Yokoyama, M. Nakano, H. Imamura, M. Yoshida, M. Tamakoshi, Rotation of the proteolipid ring in the V-ATPase. *J. Biol. Chem.* **278**, 24255–24258 (2003).
69. T. Hirata *et al.*, Subunit rotation of vacuolar-type proton pumping ATPase: Relative rotation of the *G* and *C* subunits. *J. Biol. Chem.* **278**, 23714–23719 (2003).
70. D. G. Schep, J. Zhao, J. L. Rubinstein, Models for the a subunits of the *Thermus thermophilus* V/A-ATPase and Saccharomyces cerevisiae V-ATPase enzymes by cryo-EM and evolutionary covariance. *Proc. Natl. Acad. Sci. U.S.A.* **113**, 3245–3250 (2016).
71. T. Vasanthakumar *et al.*, Structural comparison of the vacuolar and Golgi V-ATPases from *Saccharomyces pcerevisiae. Proc. Natl. Acad. Sci. U.S.A.* **116**, 7272–7277 (2019).
72. V. Leone, D. Pogoryelov, T. Meier, J. D. Faraldo-Gómez, On the principle of ion selectivity in $Na^+/H^+$-coupled membrane proteins: Experimental and theoretical studies of an ATP synthase rotor. *Proc. Natl. Acad. Sci. U.S.A.* **112**, E1057–E1066 (2015).
73. K. Schlegel, V. Leone, J. D. Faraldo-Gómez, V. Müller, Promiscuous archaeal ATP synthase concurrently coupled to $Na^+$ and $H^+$ translocation. *Proc. Natl. Acad. Sci. U.S.A.* **109**, 947–952 (2012).
74. T. Murata, K. Takase, I. Yamato, K. Igarashi, Y. Kakinuma, The *ntpJ* gene in the *Enterococcus hirae ntp* operon encodes a component of KtrII potassium transport system functionally independent of vacuolar $Na^+$-ATPase. *J. Biol. Chem.* **271**, 10042–10047 (1996).
75. R. Watanabe *et al.*, Biased Brownian stepping rotation of $F_oF_1$-ATP synthase driven by proton motive force. *Nat. Commun.* **4**, 1631 (2013).
76. W. Jiang, J. Hermolin, R. H. Fillingame, The preferred stoichiometry of *c* subunits in the rotary motor sector of *Escherichia coli* ATP synthase is 10. *Proc. Natl. Acad. Sci. U.S.A.* **98**, 4966–4971 (2001).
77. A. Wächter *et al.*, Two rotary motors in F-ATP synthase are elastically coupled by a flexible rotor and a stiff stator stalk. *Proc. Natl. Acad. Sci. U.S.A.* **108**, 3924–3929 (2011).
78. L. Colina-Tenorio, A. Dautant, H. Miranda-Astudillo, M.-F. Giraud, D. González-Halphen, The peripheral stalk of rotary ATPases. *Front. Physiol.* **9**, 1243 (2018).
79. J. E. Walker, V. K. Dickson, The peripheral stalk of the mitochondrial ATP synthase. *Biochim. Biophys. Acta* **1757**, 286–296 (2006).
80. J. Ando *et al.*, Single-nanoparticle tracking with angstrom localization precision and microsecond time resolution. *Biophys. J.* **115**, 2413–2427 (2018).